



## Reach and geometry of dynamic gas-driven fractures

Jiehao Wang<sup>a,\*</sup>, Derek Elsworth<sup>a</sup>, Yunxing Cao<sup>b</sup>, Shimin Liu<sup>a</sup>

<sup>a</sup> Department of Energy and Mineral Engineering, EMS Energy Institute and G3 Center, Pennsylvania State University, University Park, PA, 16802, USA

<sup>b</sup> Collaborative Innovation Center of Coalbed Methane and Shale Gas for Central Plains Economic Region, Henan Province, Henan Polytechnic University, 2001 Shiji Road, Jiaozuo, Henan, 454000, China

### ARTICLE INFO

#### Keywords:

Dynamic gas fracturing  
Fracture propagation  
Stress wave  
Stress intensity factor  
Multiple fractures  
High energy gas fracturing

### ABSTRACT

Dynamic gas fracturing is a well stimulation technique that is able to create multiple fractures emanating from a wellbore. It operates by pressurizing at rise-times and peak pressures intermediate between conventional hydraulic fracturing and explosive fracturing. Two consecutive processes operate during this fracturing process: (i) generation and propagation of a dynamic stress wave that overpowers the static stress field and creates multiple radial fractures around borehole, followed by (ii) quasi-static pressurization and further extension of those starter-fractures by the expanding gas. Dynamic analysis is first performed to follow the evolution of the stress wave propagating from the borehole. The radial ( $r$ ) distribution of peak tensile hoop-stress diminishes as  $1/r^\alpha$  with the power exponent ( $\alpha$ ) asymptoting to 2 as the loading rate decreases. This rapid attenuation generally limits the length of the body-wave-generated radial fractures to several borehole radii. The gas-loading of the borehole wall is followed by permeation of the gas pressure into the newly created radial fractures. Linear elastic fracture mechanics (LEFM) perturbation analysis shows that a regular distribution of multiple radial starter-cracks will preferentially propagate the longer cracks at the expense of the shorter cracks – that will arrest and snap-shut. This system naturally selects the order of six dominant fractures that may grow in unison until the *in situ* stress field reasserts control as the fractures lengthen. This restricts the maximum number of the dominant fractures to the order of six at the conclusion of treatment - a common observation in both *in situ* and laboratory experiments.

### 1. Introduction

Fractures emanating from a wellbore play a significant role in enhancing oil and gas recovery. Hydraulic fracturing, which propagates fractures at pressures slightly higher than the minimum in-situ stress and for durations greater than minutes to hours, has been a favored method to stimulate reservoirs over the last fifty years. This quasi-static pressurization typically produces a single fracture propagating perpendicular to the minimum *in situ* stress. However, since that the patterns of many of pre-existing natural fractures may also be aligned with current *in situ* stresses, the resulting hydraulic fractures may be natural-fracture-parallel and thus with limited intersection with the natural fractures.<sup>1</sup> In addition, other endemic problems of water-driven hydraulic fracturing, such as large water consumption,<sup>2</sup> activation of clays with added water,<sup>3,4</sup> and induced seismicity by reinjection of flowback fluids,<sup>5</sup> remain to be mitigated. By contrast, explosive fracturing, denoting high-strength explosives in wellbores, is sometimes applied to introduce multiple fractures by releasing extremely high energy over durations of

microseconds. However, difficulties with this relate to problems of severe wellbore damage, limited penetration away from the borehole, security risks, unpredictable results, and the creation of an impermeable cage of material under residual compression around borehole.<sup>6</sup>

Alternatively, high energy gas fracturing (HEGF) and high-pressure gas blasting/fracturing (HPGB) are two dynamic wellbore fracturing techniques that have been shown to initiate and extend multiple fractures around a borehole. High energy gas fracturing (HEGF) employs controlled burning of a propellant gas generator to achieve a tailored pressure-time behavior to fracture the formation. This method was first developed and tested by Sandia National Laboratories in late 1970s and shown to be especially promising for stimulating naturally-fractured reservoirs.<sup>1,7</sup> In contrast to HEGF, high-pressure gas blasting/fracturing (HPGB) utilizes the discharge of compressed gas after being heated to impart a high intensity and short-duration pressure spike to the wellbore wall. This is widely used in gas pre-drainage in coal seams<sup>8–10</sup> and underground excavation<sup>11</sup> and is potentially applicable to enhance oil and gas recovery due to its ability to create multiple fractures. Since

\* Corresponding author.

E-mail addresses: [jiehao.wang@psu.edu](mailto:jiehao.wang@psu.edu) (J. Wang), [elsworth@psu.edu](mailto:elsworth@psu.edu) (D. Elsworth), [yxcao17@126.com](mailto:yxcao17@126.com) (Y. Cao), [szl3@psu.edu](mailto:szl3@psu.edu) (S. Liu).

<https://doi.org/10.1016/j.ijrmms.2020.104287>

Received 3 April 2019; Received in revised form 3 March 2020; Accepted 3 March 2020

Available online 9 March 2020

1365-1609/© 2020 Elsevier Ltd. All rights reserved.

both HEGF and HPGB are dynamic stimulation tools utilizing short-duration loading by high-peak gas pressures, they are referred to as dynamic gas fracturing, herein. The principal characteristics that separate dynamic gas fracturing from hydraulic fracturing and explosive fracturing are related to loading rate and pulse duration, as depicted in Fig. 1. Generally, dynamic gas fracturing produces a much higher pressure within a much shorter duration than hydraulic fracturing but a considerably lower pressure within a longer time span than explosive fracturing.<sup>12</sup> Due to the intermediate loading rate and peak gas pressure magnitude, dynamic gas fracturing is able to create multiple fractures without the inherent disadvantages of both hydraulic and explosive fracturing.

Similar to that of explosive fracturing,<sup>13</sup> the process of dynamic gas fracturing has two consecutive stages which contribute to crack initiation and propagation: (i) generation and propagation of a stress wave driven by the rapid rise of gas pressure and (ii) quasi-static pressurization and extension of starter-fractures driven by the expanding gas. The role of the stress wave is to create initial multiple radial cracks around borehole. The peak dynamic load is typically one order of magnitude greater than the in-situ stress but below the rupture stress of the intact rock.<sup>7</sup> However, the loading rate, rather than the peak load, is the first-order effect that controls the failure behavior of the rock around the borehole.<sup>14</sup> The generation of initial multiple fractures requires an intermediate loading rate which is bounded by upper and lower limits, as demonstrated by in-situ experiments,<sup>1,7,15</sup> quasi-static stress analysis of fractured wellbores,<sup>16</sup> and dynamic calculations by numerical methods.<sup>17,18</sup> The dimensions of the resulting radial body-wave-generated cracks are determined by the transient tangential tensile stress component, rather than the radial compressive component, of the outgoing stress wave. Several dynamic analyses have been performed in order to obtain the temporal and spatial distribution of those stress components.<sup>13,19–21</sup> However, the input transient pressure pulses in those studies are limited to the specific rapid rise-times that correspond to explosive loading. The loading of the quasi-static gas pressure continues long after the stress wave has dissipated, since gas expansion rate is significantly lower than that of the propagating stress waves. This plays an important role in extending the body-wave-generated fractures and is able to increase their length by a factor of 3–100,<sup>22,23</sup> depending on the level of pressurization. Although numerous radial cracks may be formed by the propagating stress wave, only a limited population will further propagate as dominant fractures driven by gas penetration – the remainder left as dormant. This behavior is suggested by experimental observations where the number of main fractures is found to be only of the order of ~5–6.<sup>1,7,10</sup> Multiple research efforts have explored the

propagation of multiple fractures driven by the high-pressure gas penetration,<sup>22–28</sup> however, the factors that control the number, reach and hence structure and geometry of the radial fracture remain unclear.

We address this deficit in the following by exploring mechanisms of fracture initiation and growth induced by dynamic gas fracturing. This study considers an infinite homogeneous and isotropic elastic space containing a cylindrical borehole which is subjected to a transient pressure pulse followed by a quasi-static pressure. A dynamic stress analysis is first performed to explore the impact of the input pressure pulse on the length of the radial body-wave-generated cracks. This is supplemented by a stability analysis of the pressurized fractured borehole with different configurations of the radial fracture system and different degrees of gas penetration into the fractures. Although these theoretical analyses are necessarily simplified, they yield fundamental and crucial insights into controls on final geometry of the radial fractures resulting from dynamic gas fracturing.

## 2. Stress analysis of a dynamically-pressurized borehole

A dynamic stress analysis is performed to follow the propagation of the stress wave emanating from a cylindrical borehole that is subjected a transient pressure pulse. This analysis recovers the temporal and spatial distribution of the tangential tensile stress component of the stress wave, which in-turn controls the extent of the radial body-wave-generated fractures.

### 2.1. Basic equations

Consider the axisymmetric problem of an infinite homogenous and isotropic elastic medium containing a cylindrical hole of radius  $a$ , defined by the cylindrical polar co-ordinates  $r, \theta, z$  (see Fig. 2). It is assumed that the in-situ stresses are considerably smaller than the input pressure pulse and that the energy dissipation by fracturing and related damping is negligible compared to the total wave energy. Under plane strain and axisymmetric conditions, the stress-strain relations can be written as

$$\sigma_r = \frac{E(1-\nu)}{(1+\nu)(1-2\nu)} \frac{\partial u}{\partial r} + \frac{E\nu}{(1+\nu)(1-2\nu)} \frac{u}{r}, \quad (1)$$

$$\sigma_\theta = \frac{E\nu}{(1+\nu)(1-2\nu)} \frac{\partial u}{\partial r} + \frac{E(1-\nu)}{(1+\nu)(1-2\nu)} \frac{u}{r}, \quad (2)$$

in which  $\sigma_r$  and  $\sigma_\theta$  are, respectively, the radial stress and the tangential stress,  $u$  is the radial displacement, and  $E$  and  $\nu$  are the elastic modulus

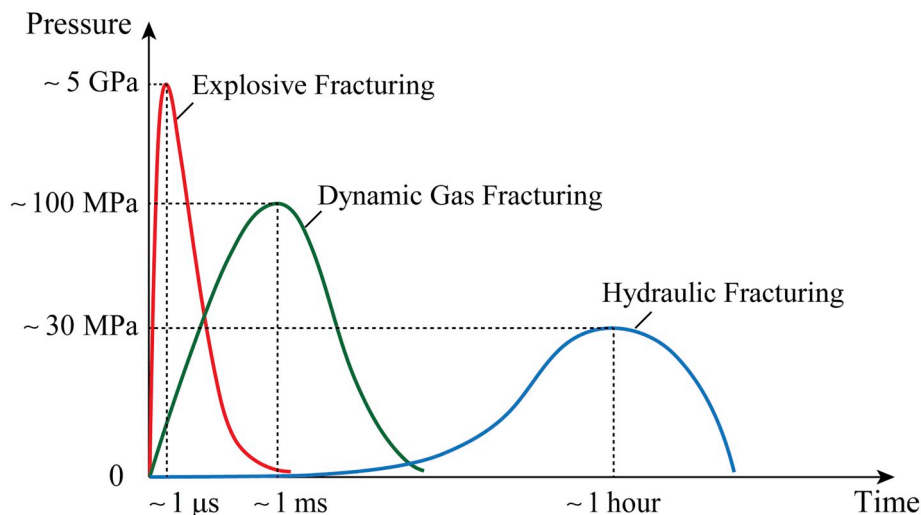


Fig. 1. Duration and magnitude of peak pressures driven by explosive fracturing, dynamic gas fracturing, and hydraulic fracturing.

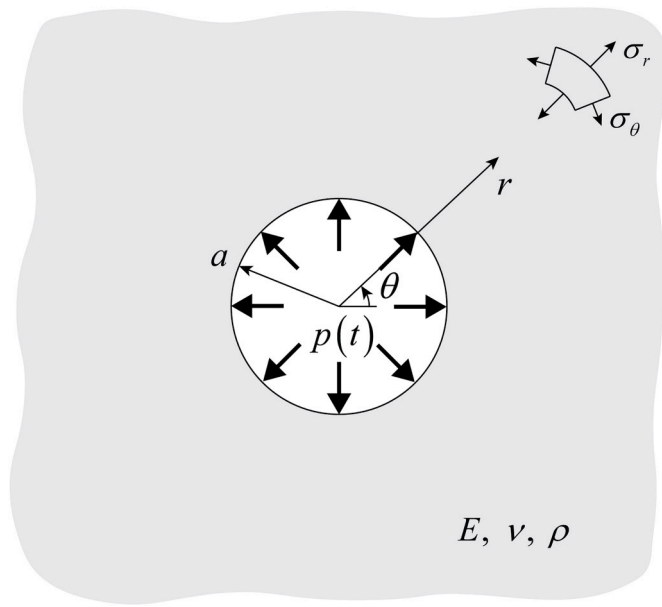


Fig. 2. Geometry, loading, and coordinates for stress wave propagation from a dynamically-pressurized infinite cylindrical hole.

and the Poisson ratio of the elastic solid, respectively. The equation of motion has the form<sup>19</sup>

$$\frac{\partial \sigma_r}{\partial r} + \frac{\sigma_r - \sigma_\theta}{r} = \rho \frac{\partial^2 u}{\partial t^2} = \frac{E(1-\nu)}{(1+\nu)(1-2\nu)} \frac{\partial^2 u}{\partial \tau^2}, \tag{3}$$

where  $t$  is the time,  $\rho$  is the density of the elastic solid, and propagation distance of the dynamic pulse in a given time is given as

$$\tau = t \left( \frac{E(1-\nu)}{(1+\nu)(1-2\nu)\rho} \right)^{1/2} \tag{4}$$

representing a space-like time coordinate. Eqs. (1)–(3) are solved for initial and boundary conditions:

$$u(r, \tau) = \dot{u}(r, \tau) = 0, \tau \leq 0, \tag{5}$$

$$\sigma_r(a, \tau) = 0, \tau \leq 0, \tag{6}$$

$$\sigma_r(a, \tau) = -p(\tau), \tau > 0, \tag{7}$$

$$\lim_{r \rightarrow \infty} [u(r, \tau)] = 0, \tau > 0, \tag{8}$$

where  $p(t)$  represents the transient pressure pulse that is applied on the wall of the circular (cylindrical) hole. The shape of the pressure pulse resulting from dynamic gas fracturing is quite complex<sup>1,7,10</sup> but is simplified here as a symmetric triangular pulse expressed as

$$p(t) = \frac{p_0}{t_0} t H(t) H(t_0 - t) + \left( 2p_0 - \frac{p_0}{t_0} t \right) H(t - t_0) H(2t_0 - t), \tag{9}$$

where  $p_0$  is the peak pressure of the pressure pulse that is reached at  $t = t_0$ , as shown in Fig. 3, and  $H(x)$  is the Heaviside step function which is equal to zero when  $x < 0$  and is equal to one when  $x \geq 0$ . Note that the pressure pulse is expressed in terms of the actual time,  $t$ , in Eq. (9) and can be rewritten as a function of the space-like time coordinate,  $\tau$ , according to Eq. (4).

### 2.2. Laplace transform solutions

Laplace transformation is introduced to eliminate the time variable in Eqs. (1)–(3) and to allow the equations to be solved in the transform

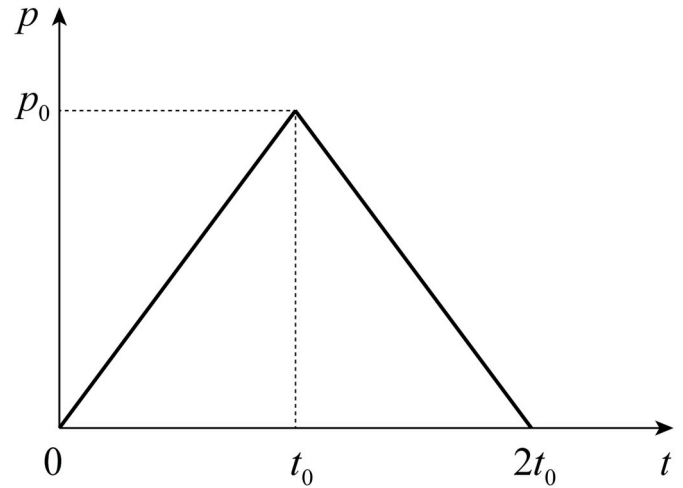


Fig. 3. Input triangular pressure pulse with a peak pressure of  $p_0$  and a pressure-rise time of  $t_0$ .

domain. The solution procedure used in this analysis follows that developed by<sup>19</sup> and is briefly summarized here. The Laplace transform of function  $f(r, \tau)$  with respect to time variable  $\tau$  denoted by  $\bar{f}(r, s)$ , is defined by

$$\bar{f}(r, s) = \int_0^\infty f(r, \tau) e^{-s\tau} d\tau \tag{10}$$

where  $s$  is the Laplace transform parameter. Therefore, Eqs. (1)–(3) are transformed to

$$\bar{\sigma}_r = \frac{E(1-\nu)}{(1+\nu)(1-2\nu)} \frac{\partial \bar{u}}{\partial r} + \frac{E\nu}{(1+\nu)(1-2\nu)} \frac{\bar{u}}{r}, \tag{11}$$

$$\bar{\sigma}_\theta = \frac{E\nu}{(1+\nu)(1-2\nu)} \frac{\partial \bar{u}}{\partial r} + \frac{E(1-\nu)}{(1+\nu)(1-2\nu)} \frac{\bar{u}}{r}, \tag{12}$$

$$\frac{\partial \bar{\sigma}_r}{\partial r} + \frac{\bar{\sigma}_r - \bar{\sigma}_\theta}{r} = \frac{E(1-\nu)}{(1+\nu)(1-2\nu)} s^2 \bar{u}, \tag{13}$$

where  $\bar{\sigma}_r(r, s)$ ,  $\bar{\sigma}_\theta(r, s)$  and  $\bar{u}(r, s)$  are the Laplace transforms of  $\sigma_r(r, \tau)$ ,  $\sigma_\theta(r, \tau)$  and  $u(r, \tau)$ , respectively. Combining Eqs. 11–13 results in the equation

$$r^2 \frac{d^2 \bar{u}}{dr^2} + r \frac{d\bar{u}}{dr} - (1 + s^2 r^2) \bar{u} = 0 \tag{14}$$

whose general solution is of the form

$$\bar{u} = A I_1(rs) + B K_1(rs) \tag{15}$$

In Eq. (14),  $I_\alpha$  and  $K_\alpha$  are the modified Bessel functions of order  $\alpha$  and of the first and second kind, respectively, and  $A$  and  $B$  are constants. Considering the boundary conditions, i.e. Eqs. (7) and (8), the constants  $A$  and  $B$  can be obtained as (see appendix for detailed derivation)

$$A = 0, \tag{16}$$

$$B = - \frac{\alpha(1+\nu)(1-2\nu)\bar{p}(s)}{EK_1(\alpha s) - \alpha s E(1-\nu)K_2(\alpha s)}, \tag{17}$$

where  $\bar{p}(s)$  is the Laplace transform of  $p(\tau)$  expressed as

$$\bar{p}(s) = \frac{p_0}{\tau_0 s^2} (e^{-\tau_0 s} - 1)^2, \tag{18}$$

with

$$\tau_0 = t_0 \left( \frac{E(1-\nu)}{(1+\nu)(1-2\nu)\rho} \right)^{1/2} \quad (19)$$

Substituting Eqs. (16) and (17) into Eq. (15) yields the solution in the Laplace domain as

$$\bar{u}(r, s) = -\frac{a(1+\nu)(1-2\nu)\bar{p}(s)K_1(rs)}{EK_1(as) - asE(1-\nu)K_2(as)} \quad (20)$$

To study the response in time domain, the Laplace domain solution, i. e. Eq. (20), is re-transformed into the time domain by using the

numerical inverse Laplace transform method proposed by.<sup>29</sup>

### 2.3. Results and discussions

For illustrative purposes, the elastic modulus, Poisson's ratio and density of the rock are selected as  $E = 25$  GPa,  $\nu = 0.25$  and  $\rho = 2500$  Kg/m<sup>3</sup>, and the radius of the hole taken as  $a = 37.5$  mm. Five rise-times of the input pressure pulse are selected as  $t_0 = 20 \mu\text{s}$ ,  $50 \mu\text{s}$ ,  $100 \mu\text{s}$ ,  $200 \mu\text{s}$  and  $2000 \mu\text{s}$  for a single peak pressure,  $p_0$ , of  $100$  MPa. Note that one reported set of *in situ* experiments<sup>23</sup> that is able to create

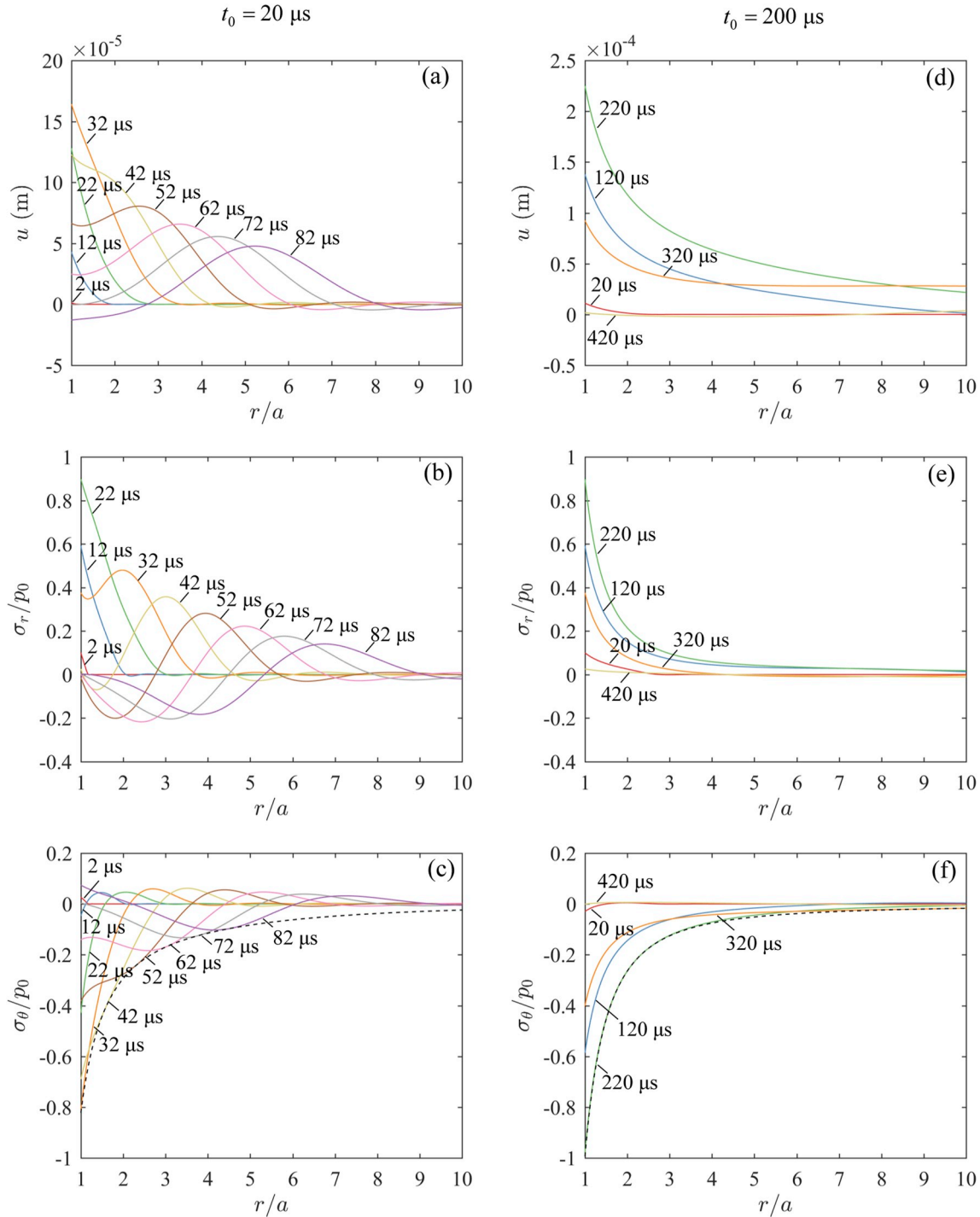


**Fig. 4.** (a) Radial displacement,  $u$ , (b) normalized radial stress,  $\sigma_r/p_0$ , and (c) normalized tangential stress,  $\sigma_\theta/p_0$ , as a function of normalized radius,  $r/a$ , for the case of  $t_0 = 20 \mu\text{s}$ ; (d) radial displacement, (e) normalized radial stress and (f) normalized tangential stress as a function of normalized radius for the case of  $t_0 = 200 \mu\text{s}$ . The dashed lines in Fig. 4(c) and (f) track the normalized tensile tangential peak,  $\sigma_{\theta\text{max}}/p_0$ , as a function of the normalized radius.

multiple fractures shows a pressure-rise-time of 500  $\mu\text{s}$  and a peak pressure of 90 MPa - comparable to the examined span of rise-times (20–2000  $\mu\text{s}$ ) and peak pressure (100 MPa) considered in this analysis.

Fig. 4 shows the radial displacement,  $u$ , normalized radial stress,  $\sigma_r/p_0$ , and normalized tangential stress,  $\sigma_\theta/p_0$ , as a function of normalized radial distance,  $r/a$ , for the two rise-times of  $t_0 = 20 \mu\text{s}$  and 200  $\mu\text{s}$ . For a rise-time of  $t_0 = 20 \mu\text{s}$ , the displacement curves clearly depict the emanating wave from the hole which begin to assume the character of the input pulse at about 52  $\mu\text{s}$  (Fig. 4(a)). The outwards displacement of the wall of the circular hole ( $r = a$ ) peaks at  $\sim 42 \mu\text{s}$  before deflating to below its original form at  $\sim 82 \mu\text{s}$ . Following this the hole again dilates and then oscillates with attenuating amplitude and increasing period for infinite time, unencumbered by damping. The radial stress is compressive at the wave-front, followed by a pronounced tensile tail with the magnitude at the hole tracking the input pressure pulse (Fig. 4(b)). Although static solutions show a tensile tangential stress, the dynamic tangential stress is first compressive before turning tensile (Fig. 4(c)) – due to the inertial constraint at the borehole wall – the tangential deformation cannot develop sufficiently quickly to enforce the equilibrium condition of zero-net-change in mean stress. This results in increased compression in the tangential direction within the thin zone affected by the stress wave. This initial compressive mode of the tangential stress is believed to be the culprit for creating both crushed zones of limited-radial-reach (instead of long radial fractures) and an impermeable skin of material under residual compression around borehole.<sup>6</sup> For a rise-time of  $t_0 = 200 \mu\text{s}$ , unlike the shorter-duration pulse, the shape of the propagating wave form is not recovered in the borehole wall (Fig. 4(d)–(f)) due to the long pressure-rise time and limited spatial extent of the window. One important feature is that the initial compressive tangential stress at the borehole wall is no longer manifest. This suggests that an input pulse with long pressure-rise time is preferred in order to minimize the residual compressive stress in the vicinity of the borehole.

The twin dashed lines of Fig. 4(c) and (f) show the normalized tensile tangential peak stress,  $\sigma_{\theta\text{max}}/p_0$ , as a function of the normalized radius. The peak tensile tangential stresses at the wall of the hole for the two cases are approximately  $0.8p_0$  and  $p_0$ , respectively, and unsurprisingly, they attenuate with increasing radius due to geometric divergence effects. Since the radial body-wave-generated fractures result from the tangential tensile stress, their anticipated extent can be approximated by assuming that the propagating fractures terminate at a radial distance where the peak tangential stress has attenuated to a value below the dynamic tensile strength of the rock. Assuming a dynamic tensile

strength of  $\sim 10\text{--}50$  MPa (slightly elevated relative to the static strength<sup>30</sup>) defines a fracture length of the order of  $0.4a\text{--}2.5a$ . Thus, it can be concluded that the length of the body-wave-generated radial cracks is quite limited and therefore penetration will rarely exceed several radii from the borehole. Fig. 5 shows the attenuation of the tensile tangential peak for all five rise-times in log-log scale. It is apparent that, in the immediate vicinity of the hole, the tensile tangential peak stress is a power function of the reciprocal of the radial distance. The power exponent is  $\sim 1.5$  for a rise-time of  $t_0 = 20 \mu\text{s}$  and increases with increasing rise-time until it reaches a peak magnitude of 2. This mirrors the tangential stress in the static solutions that is also inversely proportional to the 2nd power of the radial distance. The extent of the region that fits this power-function-relation increases with the increasing rise-time. The evolving magnitudes of the power-exponent suggest that a short pressure-rise time favors long radial cracks. However, as discussed previously, this is potentially countered by the initial compressive sense of the tangential stress that occurs with a short pressure-rise-time - which may dissipate much of the energy in the creation of a crushed zone and limit the ultimate extent of the radial fractures. This phenomenon has also been observed in several numerical simulation studies.<sup>17,31</sup>

### 3. Stability analysis of pressurized boreholes with radial cracks

After the dynamic stress wave has transited the quasi-static loading of the gas pressure on the borehole wall becomes important. These overpressures penetrate into the body-wave-generated radial fractures, potentially further propagating some of those fractures. The term “quasi-static” implies that the time-dependent pressure loading rates are sufficiently slow that the inertial effects are negligible compared to the elastic effects. We utilize Linear Elastic Fracture Mechanics (LEFM) to perform a stability analysis of the pressurized borehole that has been pre-cracked by the dynamic loading.

#### 3.1. Analysis procedure and validation

The stress intensity factor (SIF) is used in LEFM to characterize the magnitude of the singular stress field near the tip of a fracture and to define the propensity for fracture growth. Considering a plane strain problem and fractures subjected only to mode I loads, the SIF, denoted by  $K_I$ , can be related to the required energy transfer into the crack tip to drive virtual extension of the crack in its own plane, which is expressed as

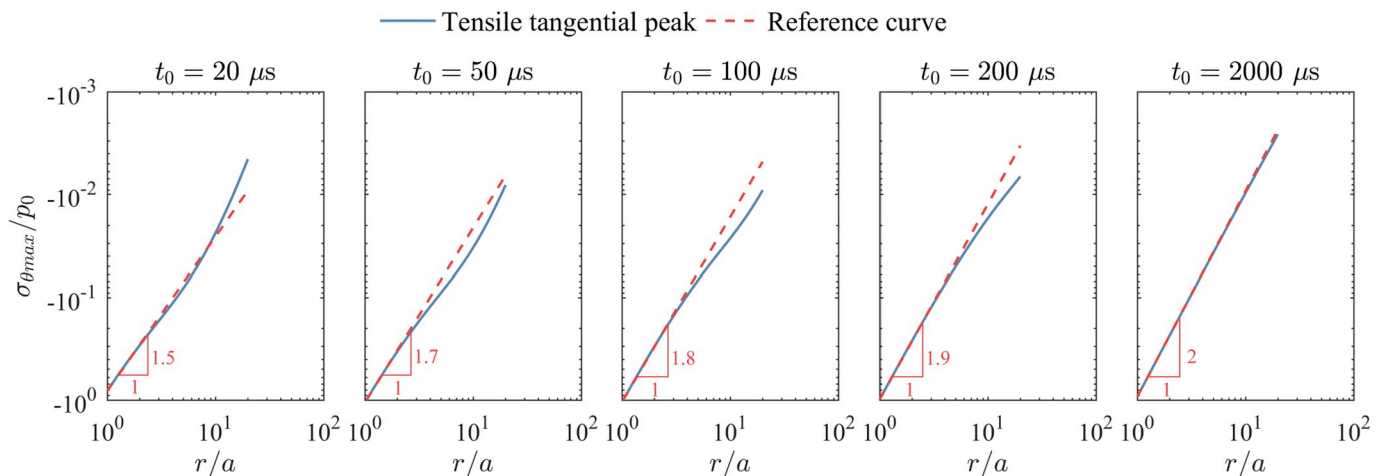


Fig. 5. Normalized tensile tangential peak stress,  $\sigma_{\theta\text{max}}/p_0$ , as a function of normalized radial distance,  $r/a$ , for the rise-times of  $t_0 = 20 \mu\text{s}$ , 50  $\mu\text{s}$ , 100  $\mu\text{s}$ , 200  $\mu\text{s}$  and 2000  $\mu\text{s}$ . The blue solid lines represent the tensile tangential peak stress, while the red dashed lines are reference curves of certain power functions with the power exponents identified in the figure. (For interpretation of the references to colour in this figure legend, the reader is referred to the Web version of this article.)

$$K_I = \sqrt{\frac{EG}{1-\nu^2}} \quad (21)$$

with

$$G = -\frac{\partial U}{\partial L}, \quad (22)$$

representing the strain energy release rate ( $G$ ), where  $L$  is the fracture length, and  $U$  is the strain energy stored in the loaded body written as

$$U = \int_V \frac{1}{2} \boldsymbol{\sigma} : \boldsymbol{\epsilon} dV \quad (23)$$

in which  $\boldsymbol{\sigma}$  is the stress tensor,  $\boldsymbol{\epsilon}$  is the strain tensor, and  $V$  is the volume of the body.

In order to calculate the SIF of a fracture of length  $L$ , the strain energy stored in the loaded body is first calculated, denoted by  $U_1$ , and a second strain energy component,  $U_2$ , is calculated after applying a small virtual extension,  $\Delta L$ , to the initial fracture. Then, the finite strain energy release rate can be approximated as

$$G = -\frac{U_2 - U_1}{\Delta L} \quad (24)$$

Finally, the SIF of the fracture can be obtained by substituting the calculated strain energy release rate ( $G$ ) into Eq. (21). The terms  $U_1$  and  $U_2$  are recovered from stress analyses for a borehole with a representative geometry containing a crack tip and using COMSOL Multiphysics finite element modeling.

This analysis procedure is validated by comparing the calculated SIF results against a known approximate expression. We consider a regular system of  $n$  radial and equally-spaced cracks of equal length  $L$  with a common origin and contained within a planar elastic medium, as shown in Fig. 6. The modeled medium extends considerably beyond the crack length, representing the infinite extent of the system. The cracks are subjected to a constant and uniformly distributed internal pressure  $p$ . Due to the intrinsic symmetry of the regular system, the SIF will be the same for all the cracks and can be adequately approximated by an expression<sup>32</sup> obtained by conformal mapping method, which is written as

$$K_I = \frac{2\sqrt{n-1}}{n} p \sqrt{\pi L}, n \geq 2 \quad (25)$$

Note that when  $n = 2$ , this crack system reduces to a classical Griffith crack of length  $2L$ , and Eq. (25) yields the exact solution

$$K_I = p \sqrt{\pi L} \quad (26)$$

A series of SIFs is calculated by this analysis procedure with the crack length ranging from 0.2 m to 2 m and the number of cracks ranging from 2 to 16. In these calculations, the elastic modulus, Poisson ratio and applied pressure are assumed to be 20 GPa, 0.25 and 20 MPa, respectively. A comparison of the calculated results against the known approximate expression (i.e. Eq. (25)) shows excellent agreement (Fig. 7).

### 3.2. Analysis

The analysis is completed on a pressurized borehole with a regular geometry of radial fractures. The distribution and geometry of the radial fractures that are created by the stress wave and further extended by gas pressure may be complex and irregular due to the heterogeneity of the material. To simplify the problem, an idealized configuration is used, as represented in Fig. 8. An even number  $n$  of equally spaced linear fractures radiate from the wall of a borehole of radius,  $a$ , with their projections passing through the center of the borehole. They have alternating lengths, with the length of one group being  $L$  and the length of the other one being  $\eta L$ , where the fracture length ratio  $\eta \geq 1$ . The analysis explores the fracture growth regime under different loading conditions and for different fracture geometries (lengths and intervals) for a simplified but representative geometry of the system.

During this stage of quasi-static gas pressurization, a gas pressure,  $p$ , is first applied on the wall of the borehole and then penetrates into the radial fractures progressively to an increasing depth,  $D$ . The gas pressure applied on the fracture walls is equivalent to that in the borehole. This is reasonable since fluid pressure only drops slightly along the high permeability portion of the opened fracture but decreases dramatically near the fluid front or constricted fracture tip.<sup>33,34</sup> The SIFs of the fractures are calculated for a combination of three penetration depths of the gas pressure (Fig. 8(b)–(d)), various (even) numbers of fractures and

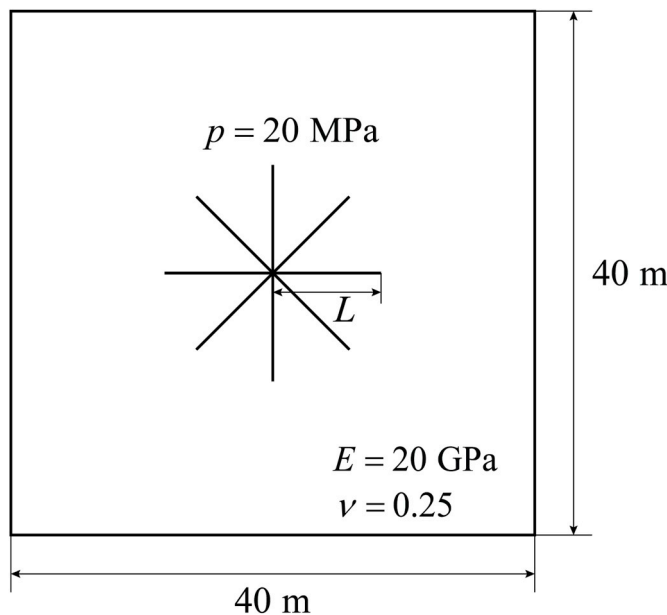


Fig. 6. Geometry of a system of radial (star-shaped) cracks used to validate the analysis procedure. Note that no wellbore is contained in this idealized system.

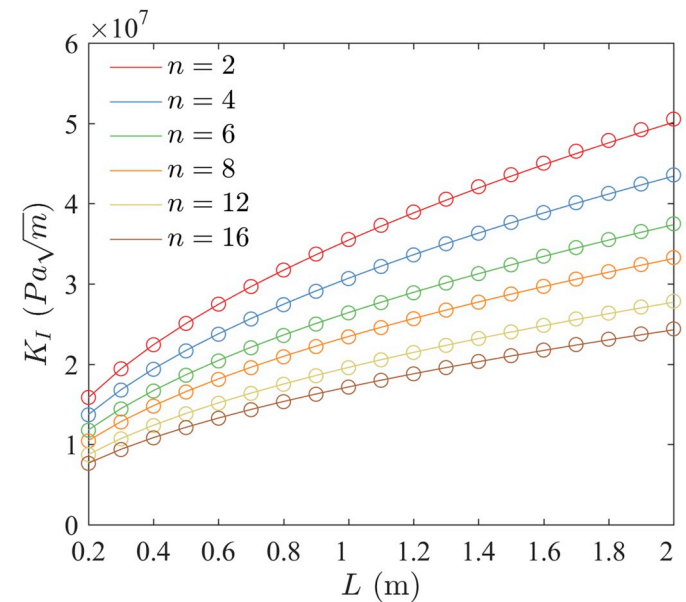
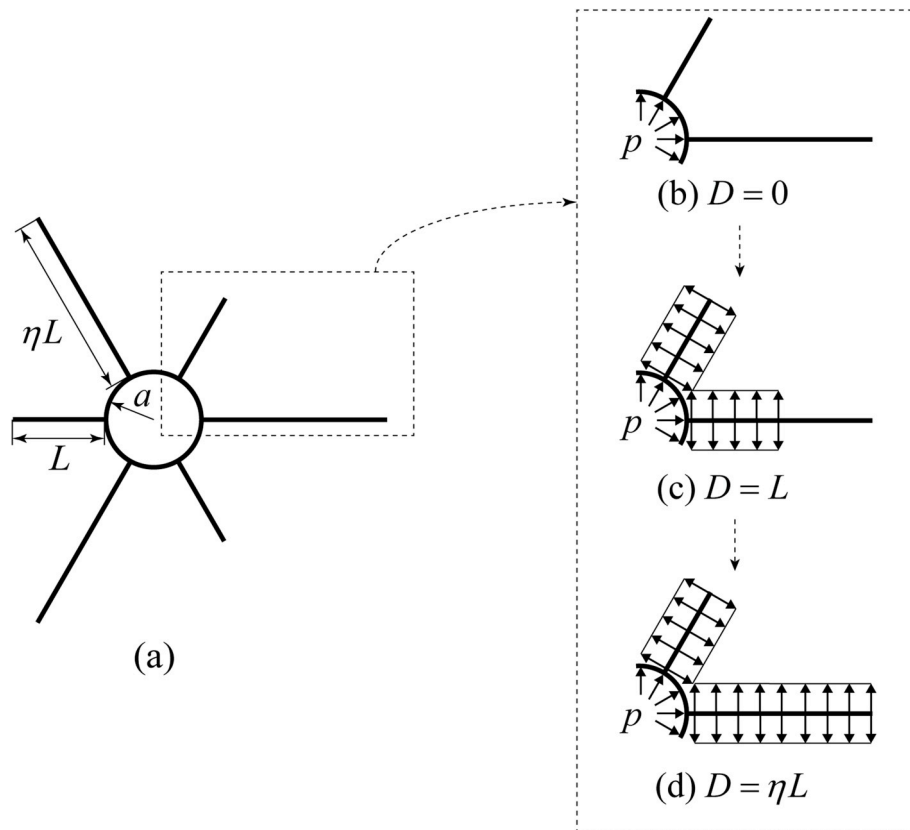


Fig. 7. Comparison of the calculated SIF (hollow circles) of a regular geometry of radial (star-shaped) cracks against a known approximate expression (solid lines) for various crack lengths and number of cracks.



**Fig. 8.** (a) An idealized configuration of a pressurized borehole with equally spaced radial fractures of alternating length, and loading conditions with different gas penetration depths (b)  $D = 0$ , (c)  $D = L$ , and (d)  $D = \eta L$ .

various fracture lengths. For the purpose of illustration, the parameters used in this analysis are assigned as those listed in Table 1.

When  $D = 0$ , the gas pressure is only applied to the wall of the borehole without any penetration into the radial fractures. Fig. 9 shows the calculated results for this loading condition with  $\eta$  ranging from 1 to 5 and  $n = 2, 4, 6$  and 8. Because of the symmetry of the geometry and loading configuration, fractures with the same length should have the same SIF, and thus only two curves of SIF are plotted in each figure. It can be seen that, when  $n = 2$ , the SIF of the shorter fracture,  $K_{IL}$ , is always larger than that of the longer fracture,  $K_{\eta L}$ . This indicates that the propagation of the shorter fracture is always favored and the fracture length coefficient,  $\eta$ , continues to decrease until the shorter fracture catches up with the longer fracture (then  $\eta = 1$ ) and then they both propagate in unison. This is not surprising, because the general fracture length dependence of the SIF under this loading configuration (i.e. the SIF is inversely proportional to the square of the fracture length) works to produce a higher SIF at the tip of the shorter fracture. However, this phenomenon is changed when this system contains four radial fractures. As observed from Fig. 9(b),  $K_{\eta L}$  is slightly larger than  $K_{IL}$  when the fracture length coefficient is in the range of  $1 < \eta < 4.2$ , which implies that the longer fractures preferentially propagate instead of the shorter ones when their difference is small. The shorter fractures recover this

priority when  $\eta > 4.2$ . Thus, the fracture length coefficient may eventually remain constant at  $\eta = 4.2$ . A possible reason for this is that the longer fractures undergo a larger opening than the shorter fractures, clamping the entry to the smaller fracture and reducing the circumferential stresses that would dilate the shorter fractures. There is a competition between this compressive clamping effect and the general fracture length dependence of the SIF, with the former one prevailing at  $1 < \eta < 4.2$  and the latter one dominating at  $\eta > 4.2$ . The compressive clamping effect becomes more pronounced as the system contains more fractures. It can be seen from Fig. 9(c) and (d) that, when  $n = 6$  and 8,  $K_{\eta L}$  is considerably higher than  $K_{IL}$  for any value of  $\eta$  and  $K_{IL}$  decreases quite rapidly with increasing  $\eta$ . This indicates that the clamping effect dominates all the time and works in favor of the propagation of the longer fractures. Therefore, for a system containing  $n \geq 4$  fractures and without gas penetration, propagation of the longer fractures and suppression of the shorter fractures are always expected (except for the condition of  $n = 4$  and  $\eta \geq 4.2$ ), and consequently, uniform growth of the configuration seems impossible. This will be the case, even when the excess length of the longer fractures is infinitesimally small, i.e. as  $\eta$  approaches unity. This is apparent in Fig. 9 as SIF for the longer fracture is always greater than that for the shorter fracture for  $n > 4$  even as  $\eta \rightarrow 1$ .

The gas penetration depth  $D = L$  represents the situation where the shorter and longer fractures are alternately fully and partially pressurized, respectively (see Fig. 8(c)). A series of SIFs are calculated for  $1 \leq \eta \leq 5$  and  $n = 2, 4, 6, 8, 10$  and 12, as shown in Fig. 10. It is interesting to observe that  $K_{IL}$  is relatively larger than  $K_{\eta L}$  when  $n = 2, 4$  and 6, suggesting a uniform growth of the configuration. This results from the fact that the clamping effect is counteracted by the gas pressure which fully fills the shorter fractures. The fracture growth behavior becomes complex as more fractures are involved ( $n = 8, 10$  and 12) under this loading configuration. As illustrated in Fig. 10 (d), (e) and 10(f), the two curves for  $K_{IL}$  and  $K_{\eta L}$  cross at two points,

**Table 1**

Parameters used in the analysis of a pressurized borehole with radial cracks.

Parameters	Values
Elastic modulus of the solid, $E$	20 GPa
Poisson ratio of the solid, $\nu$	0.25
Radius of the borehole, $a$	0.1 m
Gas pressure, $p$	60 MPa
Fracture length, $L$	0.4 m

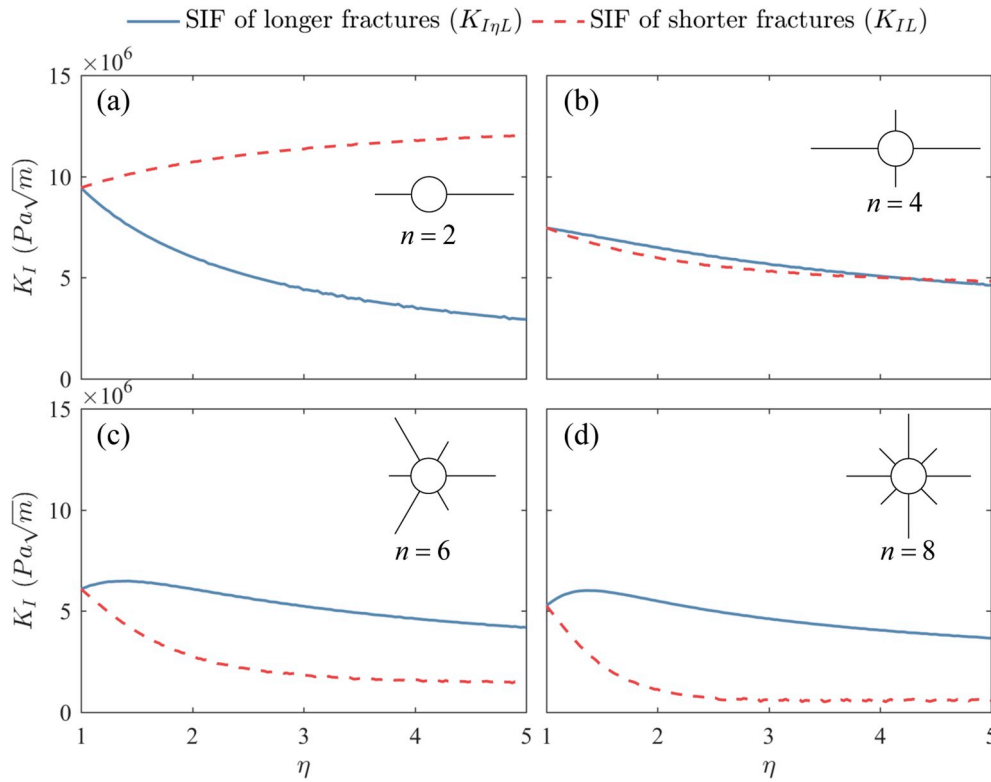


Fig. 9. Calculated SIFs as functions of fracture length coefficient,  $\eta$ , without gas penetration for (a)  $n = 2$ , (b)  $n = 4$ , (c)  $n = 6$ , and (d)  $n = 8$ . The blue solid lines represent the SIFs of longer fractures,  $K_{I\eta L}$ , while the red dashed lines represent the SIFs of shorter fractures,  $K_{IL}$ . (For interpretation of the references to colour in this figure legend, the reader is referred to the Web version of this article.)

namely  $\eta = \eta_1$  and  $\eta = \eta_2$ , which divide the curves into three parts. It is apparent that uniform propagation occurs in the interval  $1 < \eta < \eta_1$  while non-uniform propagation is preferred in the intervals  $\eta_1 < \eta < \eta_2$  and  $\eta > \eta_2$ . However, it is noted that the magnitude of  $\eta_1$  is generally less than 1.3 which is relatively small. As a result, it is possible for a value of  $\eta$ , which is originally  $1 < \eta < \eta_1$  and favors uniform propagation, to exceed  $\eta_1$  and shift into the interval  $\eta_1 < \eta < \eta_2$ , considering the heterogeneity of the material and possible non-ideal loading. This imbalance will then be amplified continuously and result in a final value of  $\eta$  which is around 4.

As the gas further penetrates, all the fractures may fully fill and be subjected to a uniform gas pressure, corresponding to the penetration depth  $D = \eta L$ . Fig. 11 shows the resulting SIFs for  $1 \leq \eta \leq 3$  and  $n = 2, 4, 6, 8, 10$  and 12. Non-uniform growth of the configuration is always expected under this loading condition for  $n \geq 4$  because  $K_{I\eta L}$  is considerably larger than  $K_{IL}$  (see Fig. 11). One key reason for this is the fracture length dependence of the SIF for the fully pressurized fractures since the SIF is proportional to the square of the fracture length. This is contrary to the zero gas penetration condition and suggests that the longer fractures experience larger SIFs. Additionally, the compressive clamping effect is intensified by the uniformly applied pressure on the wall of the longer fractures, further decreasing the SIF of the shorter fractures. It is also interesting to note that  $K_{IL}$  may decrease to zero when  $n \geq 6$ , indicating that tip closure of the shorter fractures may occur even for moderately imbalanced lengths. For the case of  $n = 2$ , it is observed that the SIFs for the longer and shorter fractures are exactly identical. This is intuitively accepted since, when only two fractures exist in this system, these two fractures can be viewed as a single longer fracture subjected to a uniform internal pressure, and thus, the two fracture tips naturally experience the same SIF. This could be one reason why a symmetric bi-wing fracture is always produced during the conventional hydraulic fracturing.

These three idealized gas penetration depths represent three end-

member conditions of the fracture growth regime, with the other gas penetration depths resulting in intermediate fracture growth regimes transiting between them. A possible process of fracture propagation during dynamic gas fracturing is illustrated in Fig. 12. The stress wave may create numerous radial fractures. However, immediately after the initiation of quasi-static gas pressurization, the system of the fractures exists in the non-uniform growth regime due to null or limited gas penetration. Small initial imbalances, which might result from material heterogeneity and non-ideal loading, will always be amplified, and thus only a few of the fractures are able to propagate significantly and the number of dominant fractures will progressively decrease until it is less than four. After the gas has penetrated to a critical depth from the borehole, the system transits into a regime of uniform fracture growth which allows up to six dominant fractures to maintain a similar length and propagate at a similar rate. In this regime, if more than six fractures exist in this system, the number of the dominant fractures might be exactly six. As the gas continuously penetrates deeper, the system will transit back into the regime of non-uniform fracture growth. In this, the six dominant fractures in the previous stage begin to be differentiated in length, with the propagation of a small number (possibly two) of them being favored and with the others arresting. As a consequence, the number of dominant large fractures should not exceed six at the end of the treatment. Those dominant fractures will tend to be approximately equally spaced, since this configuration dissipates the least energy during fracturing process because the least clamping effect is endured.

We note that this response is analogous to the generation of dominant cracks from the surface of a half-space that shrinks as a result of drying or cooling at the surface.<sup>35-37</sup> In this, an infinite number of starter cracks will grow as tensile stresses exceed the tensile strength of the surface, before every second crack arrests as the intervening crack dominates the local stress regime. The favored cracks continue to grow, until the tip-local stress fields again mutually-interfere as the crack lengths grow, when again every other crack will arrest and the

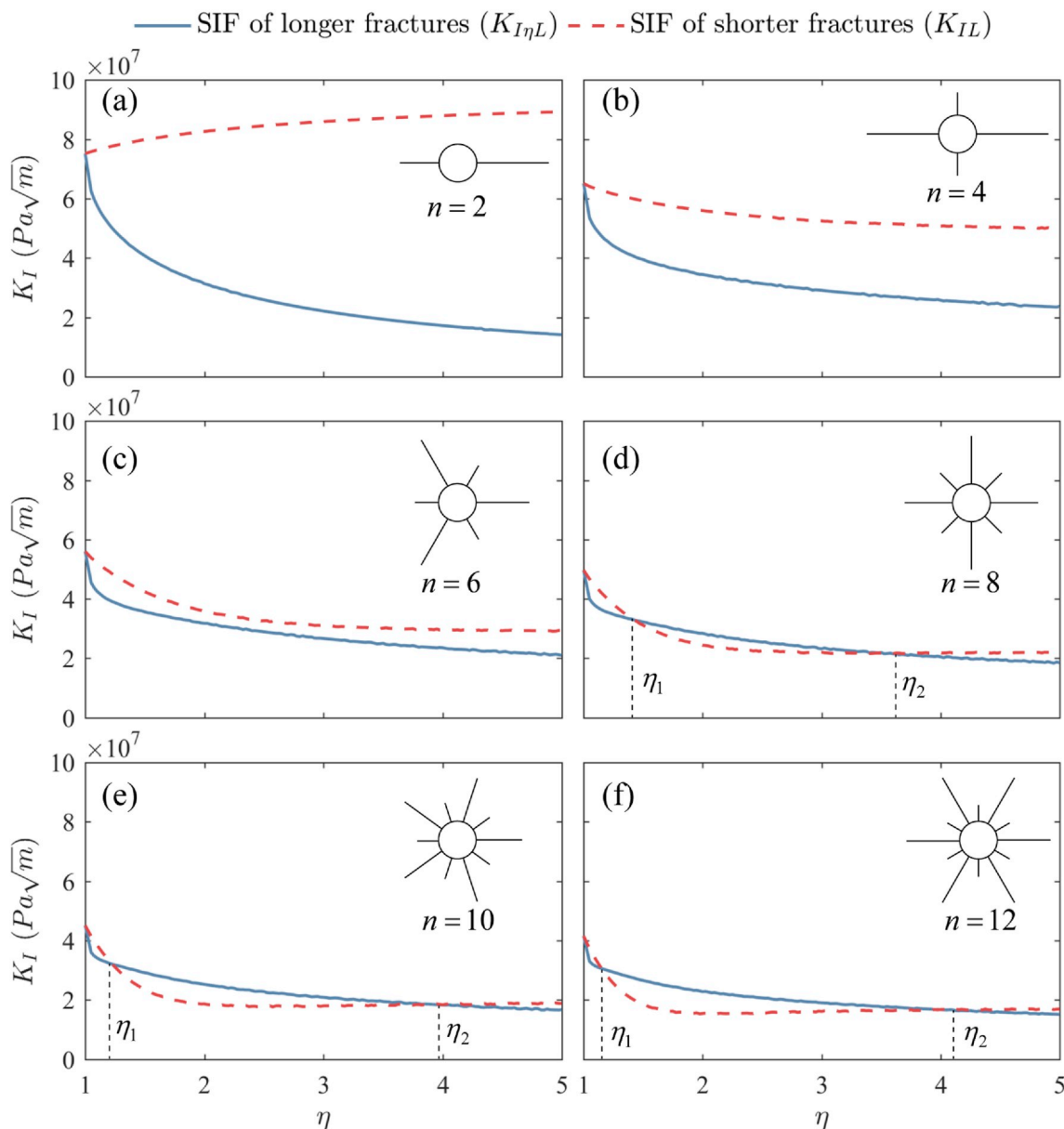


**Fig. 10.** Calculated SIFs as functions of fracture length coefficient,  $\eta$ , with gas penetration depth of  $D = L$  for (a)  $n = 2$ , (b)  $n = 4$ , (c)  $n = 6$ , (d)  $n = 8$ , (e)  $n = 10$ , and (f)  $n = 12$ . The blue solid lines represent the SIFs of the longer fractures,  $K_{I\eta L}$ , while the red dashed lines represent the SIFs of the shorter fractures,  $K_{IL}$ . (For interpretation of the references to colour in this figure legend, the reader is referred to the Web version of this article.)

intervening dominant cracks growing further. This behavior continues to develop a power-law self-similar distribution of cracks with a few dominant cracks and nested families of progressively smaller-length fractures.

The parameters used in the calculations (Table 1) have little influence on the results of the analysis discussed above, as long as the length of the radial fractures is larger than twice the radius of the borehole.<sup>26</sup> Note that, by assuming a sufficiently high gas pressure, the solid body is considered as free from far-field stresses. However, when in-situ stresses are taken into account, the physical process will become much more complex, and during this process, the fractures may curve and gradually align with the *in situ* stresses where *in situ* stress effect become dominant as gas pressure effects wane. In addition, pre-existing natural fractures are not taken into consideration in this study but could also impact the evolving geometry of the fracture system by changing fracture propagation directions or even arresting fracture propagation.<sup>38,39</sup> Admittedly these are oversimplifications, however, in view of the analytical

difficulties, this analysis is adequate to bring into focus some of the delicate and crucial considerations that are required to predict the final geometry of the fractures resulting from dynamic gas fracturing. Finally, it should be noted that the results presented in this section can also be applied to some other related problems, such as explosive fracturing,<sup>13</sup> pulse hydraulic fracturing,<sup>40</sup> and fracturing by non-explosive expansion.<sup>41</sup>

#### 4. Conclusions

Dynamic gas fracturing involves mechanisms of fracturing in two largely separate and consecutive stages which contribute to crack initiation and propagation. This involves: (i) transit of the solid body stress wave, induced by rapid rise of gas pressure within the borehole and creating initial multiple radial fractures, and (ii) the application of quasi-static pressure of the expanding gas further extending the body-wave-generated fractures. In order to determine the final geometry of

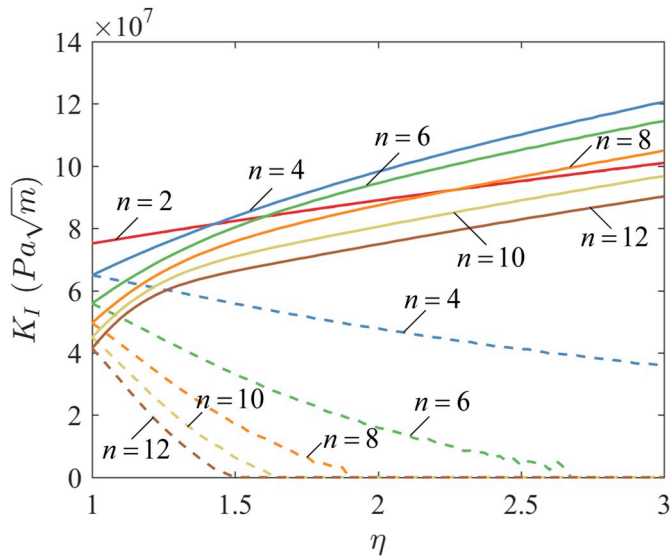


Fig. 11. Calculated SIFs as functions of fracture length coefficient,  $\eta$ , with full gas penetration for  $n = 2, 4, 6, 8, 10$  and  $12$ . The blue solid lines represent the SIFs of longer fractures,  $K_{I,pl}$ , while the red dashed lines represent the SIFs of shorter fractures,  $K_{I,l}$ . (For interpretation of the references to colour in this figure legend, the reader is referred to the Web version of this article.)

the fractures induced by dynamic gas fracturing, a dynamic stress analysis is first performed to explore the impact of the input pressure pulse on the length of the radial body-wave-generated cracks, which is followed by a stability analysis of pressurized fractures propagating from the borehole with different configurations of the radial fracture system (length distribution and number) and different degrees of gas penetration into the individual fractures.

The dynamic stress analysis is completed by solving the radial wave equation via Laplace transform. This returns the temporal and spatial distributions of the tangential tensile stress resulting from symmetric triangular rise- and decay-time pressure pulses applied to the borehole wall. This loading plays a decisive role in determining the extent of the

radial wave-generated fractures. Results show that short pressure-rise times accompany initial compressive tangential stress that is posited to be the cause of the impermeable cage of material sometimes implied from residual compression around borehole. This initial compressive feature disappears as the pressure-rise time increases. The radial ( $r$ ) distribution of peak tensile hoop-stress diminishes as  $1/r^\alpha$  with the power exponent ( $\alpha$ ) asymptoting to 2 as the loading rate decreases. By applying the maximum tensile stress criterion to these obtained power functions, it is found that the length of the body-wave-generated radial cracks is quite limited and usually does not penetrate outwards any further than several borehole radii.

After the stress wave has dissipated, high-pressure gas is able to expand quasi-statically into the body-wave-generated fractures. Stress intensity factors are calculated for these fractures using finite element-based stress analysis. A variety of different fracture growth regimes are observed with the gas penetration. These result from the interaction between the general fracture length dependency of the stress intensity factor and the compressive clamping effect. When gas penetration is limited, a regime of non-uniform fracture growth is expected with only a few (possibly less than four) of those body-wave-generated fractures able to extended noticeably. After the gas has penetrated to a critical depth along the fractures, the system transits into a regime of uniform fracture growth which allows up to six dominant fractures to maintain a similar length and propagate at a similar rate. As the gas continues to penetrate, the system gradually transits back into the non-uniform fracture growth regime, which favors the propagation of only a fraction of the six dominant fractures observed to propagate in the previous stage. Therefore, the number of the dominant fractures at the conclusion of the treatment is unlikely to exceed six. Additionally, these resulting dominant fractures are likely to be approximately equally spaced, since this configuration dissipates the least energy during fracturing since the least clamping effect is apparent.

**Declaration of competing interest**

The authors declare that they have no known competing financial interests or personal relationships that could have appeared to influence the work reported in this paper.

**Appendix Derivation of particular solution to Eq. (14)**

Eq. (15) is the general solution to Eq. (14) and is repeated here for convenience,

$$\bar{u} = A I_1(rs) + B K_1(rs) \tag{A1}$$

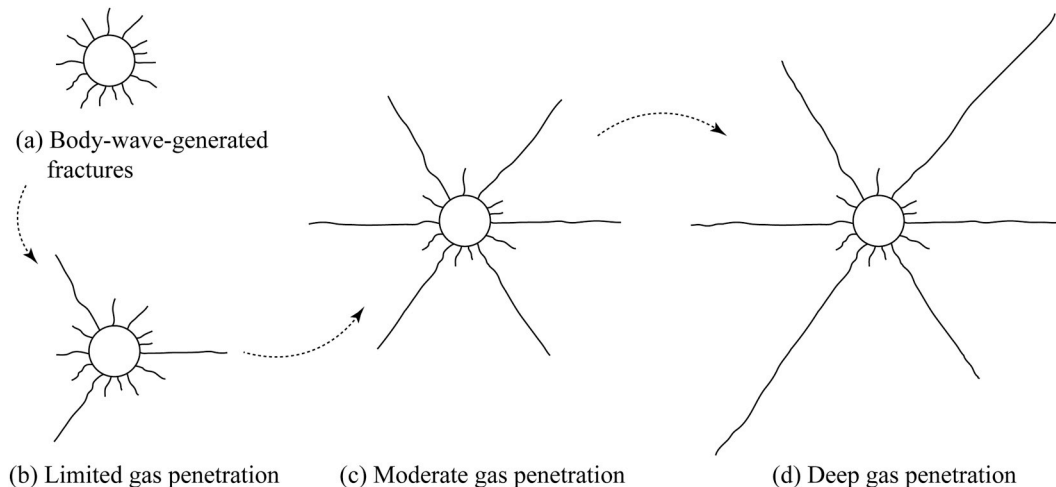


Fig. 12. Suggested hierarchy of limiting processes contributing to fracture propagation during dynamic gas fracturing.

where  $I_\alpha$  and  $K_\alpha$  are the modified Bessel functions of order  $\alpha$  and of the first and second kind, respectively, and  $A$  and  $B$  are constants.

The Laplace transform of the boundary conditions, i.e. Eqs. (7) and (8), can be written as

$$\bar{\sigma}_r(a, s) = -\bar{p}(s), \tag{A2}$$

$$\lim_{r \rightarrow \infty} [\bar{u}(r, s)] = 0, \tag{A3}$$

where  $\bar{p}(s)$  is given by Eq. (18).

Substituting Eq. (A3) into Eq. (A1) yields

$$\lim_{r \rightarrow \infty} [AI_1(rs) + BK_1(rs)] = 0 \tag{A4}$$

However, functions  $I_1(z)$  and  $K_1(z)$  approach infinity and zero, respectively, as  $z$  goes to infinity (see Fig. A1). Thus, we must have

$$A = 0, \tag{A5}$$

in order to fulfill the requirement of Eq. (A4).

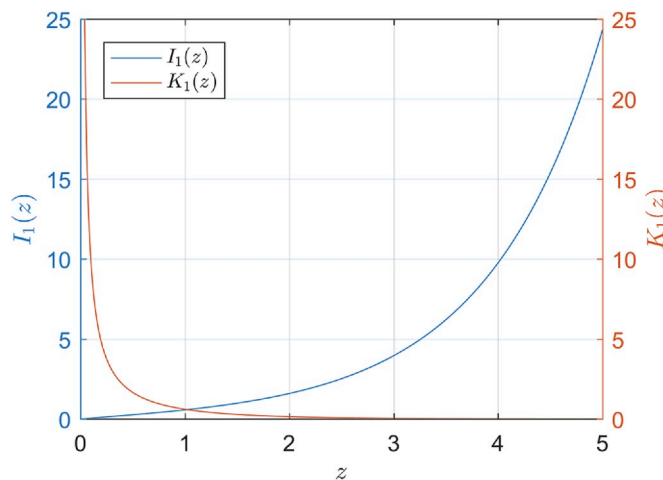


Fig. A1. Modified Bessel functions of the first and second kind for  $\alpha = 1$ .

Substituting Eq. (A1) and (A5) into Eq. (11) gives

$$\begin{aligned} \bar{\sigma}_r(r, s) &= \frac{BE(1-\nu)}{(1+\nu)(1-2\nu)} \frac{\partial K_1(rs)}{\partial r} + \frac{BE\nu}{(1+\nu)(1-2\nu)} \frac{K_1(rs)}{r} \\ &= \frac{BE(1-\nu)}{(1+\nu)(1-2\nu)} \left[ \frac{K_1(rs)}{r} - sK_2(rs) \right] + \frac{BE\nu}{(1+\nu)(1-2\nu)} \frac{K_1(rs)}{r} \\ &= B \frac{EK_1(rs) - rsE(1-\nu)K_2(rs)}{(1+\nu)(1-2\nu)r} \end{aligned} \tag{A6}$$

Applying the boundary condition of Eq. (A2) to Eq. (A6) yields

$$B = - \frac{a(1+\nu)(1-2\nu)\bar{p}(s)}{EK_1(as) - asE(1-\nu)K_2(as)} \tag{A7}$$

Therefore, the particular solution to Eq. (14) can be obtained by substituting Eq. (A5) and (A7) into Eq. (A1) as

$$\bar{u}(r, s) = - \frac{a(1+\nu)(1-2\nu)\bar{p}(s)K_1(rs)}{EK_1(as) - asE(1-\nu)K_2(as)} \tag{A8}$$

**Appendix A. Supplementary data**

Supplementary data to this article can be found online at <https://doi.org/10.1016/j.ijrmms.2020.104287>.

**References**

- Schmidt RA, Warpinski NR, Cooper PW. In situ evaluation of several tailored-pulse well-shooting concepts. In: *SPE Unconventional Gas Recovery Symposium*. Society of Petroleum Engineers; 1980:105–111. <https://doi.org/10.2118/8934-MS>.
- Vengosh A, Jackson RB, Warner N, Darrah TH, Kondash A. *Risks to Water Resources from Shale Gas Development and Hydraulic Fracturing in the United States*. vol. 16. 2014: 6838.
- Middleton RS, Carey JW, Currier RP, et al. Shale gas and non-aqueous fracturing fluids: opportunities and challenges for supercritical CO<sub>2</sub>. *Appl Energy*. 2015;147: 500–509. <https://doi.org/10.1016/j.apenergy.2015.03.023>.

- 4 Wang J, Elsworth D, Wu Y, Liu J, Zhu W, Liu Y. The influence of fracturing fluids on fracturing processes: a comparison between water, oil and SC-CO<sub>2</sub>. *Rock Mech Rock Eng.* 2018;51:299–313. <https://doi.org/10.1007/s00603-017-1326-8>.
- 5 Elsworth D, Spiers CJ, Niemeijer AR. Understanding induced seismicity. *Science.* 2016;350(6354):1380–1381. <https://doi.org/10.1126/science.aal2584>.
- 6 Schmidt RA, Boade RR, Bass RC. A new perspective on well shooting-behavior of deeply buried explosions and deflagrations. *J Petrol Technol.* 1981;33:1305–1311. <https://doi.org/10.2118/8346-PA>.
- 7 Warpinski NR, Schmidt RA, Cooper PW, Walling HC, Northrop DA, High A. High-energy gas Frac : multiple fracturing in a wellbore. In: *20th US Symposium on Rock Mechanics.* American Rock Mechanics Association; 1979:143–148.
- 8 Cao Y, Zhang J, Zhai H, Fu G, Tian L, Liu S. CO<sub>2</sub> gas fracturing: a novel reservoir stimulation technology in low permeability gassy coal seams. *Fuel.* 2017;203:197–207. <https://doi.org/10.1016/j.fuel.2017.04.053>.
- 9 Chen H, Wang Z, Chen Xien, Chen Xiangjun, Wang L. Increasing permeability of coal seams using the phase energy of liquid carbon dioxide. *J CO<sub>2</sub> Util.* 2017;19:112–119. <https://doi.org/10.1016/j.jcou.2017.03.010>.
- 10 Zhu WC, Gai D, Wei CH, Li SG. High-pressure air blasting experiments on concrete and implications for enhanced coal gas drainage. *J Nat Gas Sci Eng.* 2016;36:1253–1263. <https://doi.org/10.1016/j.jngse.2016.03.047>.
- 11 Singh SP. Non-explosive applications of the PCF concept for underground excavation. *Tunn Undergr Space Technol.* 1998;7:798:305–311. [https://doi.org/10.1016/S0886-7798\(98\)00062-5](https://doi.org/10.1016/S0886-7798(98)00062-5).
- 12 Jaimes M, Castillo RD, Mendoza SA. High energy gas fracturing: a technique of hydraulic prefracturing to reduce the pressure losses by friction in the near wellbore - a Colombian field application. *SPE Lat Am Caribb Pet Eng Conf.* 2012. <https://doi.org/10.2118/152886-MS>.
- 13 Kutter HK, Fairhurst C. On the fracture process in blasting. *Int J Rock Mech Min Sci.* 1971;8:181–202. [https://doi.org/10.1016/0148-9062\(71\)90018-0](https://doi.org/10.1016/0148-9062(71)90018-0).
- 14 Chu TY, Warpinski N, Jacobson RD. In situ experiments of geothermal well stimulation using gas fracturing technology. *Sandia Natl Lab Rep.* 1988.
- 15 Cuderman JF. Design and modeling of small- scale multiple-fracturing experiments. *Sandia Natl Lab Rep.* 1981.
- 16 Warren WE. The quasi-static stress field around a fractured well bore. *Int J Fract.* 1982;18:113–124. <https://doi.org/10.1007/BF00019636>.
- 17 Cho SH, Kaneko K. Influence of the applied pressure waveform on the dynamic fracture processes in rock. *Int J Rock Mech Min Sci.* 2004;41:771–784. <https://doi.org/10.1016/j.ijrmms.2004.02.006>.
- 18 Ma GW, An XM. Numerical simulation of blasting-induced rock fractures. *Int J Rock Mech Min Sci.* 2008;45:966–975. <https://doi.org/10.1016/j.ijrmms.2007.12.002>.
- 19 Eason G. Propagation of waves from spherical and cylindrical cavities. *J Appl Math Phys.* 1963;14:12–23. <https://doi.org/10.1007/BF01601142>.
- 20 Selberg HL. Transient compression waves from spherical and cylindrical cavities. *Arkiv Fysik.* 1952;5:97–108.
- 21 Sharpe JA. The production of elastic waves by explosion pressures. I. Theory and empirical field observations. *Geophysics.* 1942;7:144–154.
- 22 McHugh S. Crack extension caused by internal gas pressure compared with extension caused by tensile stress. *Int J Fract.* 1983;21:163–176. <https://doi.org/10.1007/BF00963386>.
- 23 Nilson RH, Proffer WJ, Duff RE. Modelling of gas-driven fractures induced by propellant combustion within a borehole. *Int J Rock Mech Min Sci.* 1985;22:3–19. [https://doi.org/10.1016/0148-9062\(85\)92589-6](https://doi.org/10.1016/0148-9062(85)92589-6).
- 24 Goodarzi M, Mohammadi S, Safari A. Numerical analysis of rock fracturing by gas pressure using the extended finite element method. *Petrol Sci.* 2015;12:304–315. <https://doi.org/10.1007/s12182-015-0017-x>.
- 25 Nilson R, Griffiths S. Similarity analysis of energy transport in gas-driven fractures. *Int J Fract.* 1986;30:115–134. <https://doi.org/10.1007/BF00034021>.
- 26 Ouchterlony F. Fracture mechanics applied to rock blasting. In: *Congress of the International Society for Rock Mechanics.* 1974:1377–1383.
- 27 Paine AS, Please CP. An improved model of fracture propagation by gas during rock blasting - some analytical results. *Int J Rock Mech Min Sci Geomech Abstr.* 1994;31:699–706. [https://doi.org/10.1016/0148-9062\(94\)90009-4](https://doi.org/10.1016/0148-9062(94)90009-4).
- 28 Il Sim Y, Cho GC, Song K. Prediction of fragmentation zone induced by blasting in rock. *Rock Mech Rock Eng.* 2017;50:2177–2192. <https://doi.org/10.1007/s00603-017-1210-6>.
- 29 Stehfest H. Numerical inversion of Laplace transforms algorithm 368. *Commun ACM.* 1970;13:47–49.
- 30 Qian Q, Qi C, Wang M. Dynamic strength of rocks and physical nature of rock strength. *J Rock Mech. Geotech. Eng.* 2009;1:1–10. <https://doi.org/10.3724/SP.J.1235.2009.00001>.
- 31 Donzé FV, Bouchez J, Magnier SA. Modeling fractures in rock blasting. *Int J Rock Mech Min Sci.* 1997;34:1153–1163. [https://doi.org/10.1016/S1365-1609\(97\)80068-8](https://doi.org/10.1016/S1365-1609(97)80068-8).
- 32 Ouchterlony F. Stress intensity factors for the expansion loaded star crack. *Eng Fract Mech.* 1976;8:447–448.
- 33 Wang J, Elsworth D, Denison MK. Propagation, proppant transport and the evolution of transport properties of hydraulic fractures. *J Fluid Mech.* 2018;855:503–534. <https://doi.org/10.1017/jfm.2018.670>.
- 34 Wang J, Elsworth D, Denison MK. Hydraulic fracturing with leakoff in a pressure-sensitive dual porosity medium. *Int J Rock Mech Min Sci.* 2018;107:55–68. <https://doi.org/10.1016/j.ijrmms.2018.04.042>.
- 35 Keer LM, Nemat-Nasser S, Oranratnachai A. Unstable growth of thermally induced interacting cracks in brittle solids: further results. *Int J Solid Struct.* 1979;15:111–126. [https://doi.org/10.1016/0020-7683\(79\)90016-7](https://doi.org/10.1016/0020-7683(79)90016-7).
- 36 Nemat-Nasser S, Keer LM, Parihar HS. Unstable growth of thermally induced interacting cracks in brittle solids. *Int J Solid Struct.* 1978;14:409–430. [https://doi.org/10.1016/0020-7683\(78\)90007-0](https://doi.org/10.1016/0020-7683(78)90007-0).
- 37 Nemat-Nasser S, Oranratnachai A. Minimum spacing of thermally induced cracks in brittle solids: addendum. *J Energy Resour Technol Trans ASME.* 1982;104:96–98. <https://doi.org/10.1115/1.3446859>.
- 38 Zhang F, Damjanac B, Maxwell S. Investigating hydraulic fracturing complexity in naturally fractured rock masses using fully coupled multiscale numerical modeling. *Rock Mech Rock Eng.* 2019;52:5137–5160. <https://doi.org/10.1007/s00603-019-01851-3>.
- 39 Zhang F, Dontsov E, Mack M. Fully coupled simulation of a hydraulic fracture interacting with natural fractures with a hybrid discrete-continuum method. *Int J Numer Anal Methods Geomech.* 2017;41:1430–1452. <https://doi.org/10.1002/nag.2682>.
- 40 Li Q, Lin B, Zhai C. The effect of pulse frequency on the fracture extension during hydraulic fracturing. *J Nat Gas Sci Eng.* 2014;21:296–303. <https://doi.org/10.1016/j.jngse.2014.08.019>.
- 41 Zhai C, Xu J, Liu S, Qin L. Fracturing mechanism of coal-like rock specimens under the effect of non-explosive expansion. *Int J Rock Mech Min Sci.* 2018;103:145–154. <https://doi.org/10.1016/j.ijrmms.2018.01.037>.